ACS OMEGA

Open Access

This article is licensed under CC-BY-NC-ND 4.0

http://pubs.acs.org/journal/acsodf

Article

# Effect of Gentamicin-Loaded Calcium Phosphate Coating and Polymeric Coating on the Degradation Properties of Biodegradable Iron-Based Biomaterials

Martina Petráková, Radka Gorejová, Jana Shepa, Ján Macko, Miriam Kupková, Ondrej Petruš, Matej Baláž, Tibor Sopčák, Matej Mičušík, Martin Kožár, Vanda Hajdučková, and Renáta Oriňaková*

Cite This: *ACS Omega* 2024, 9, 48299−48314

Read Online

ACCESS | Metrics & More | Article Recommendations

**ABSTRACT:** In the past decades, iron has been one of the intensively studied biodegradable metals due to its suitable mechanical properties, but it suffers from slow degradation in a physiological environment and low bioactivity. In this work, the beneficial properties of ceramic and polymer coatings were merged to enhance the corrosion properties and biological compatibility of Fe-based biomaterials. A new bilayer coating for Fe-based biomaterials that speeds up degradation while offering controlled, localized drug release to prevent infections was prepared. In addition, bioactive coatings with an incorporated antibiotic (gentamicin, Ge) were produced to introduce antibacterial properties into the prepared biomaterials and thus increase their bioactivity. The calcium phosphate (CaP) coating layer as well as a bioactive coating layer of CaP doped with gentamicin was electrochemically deposited onto an iron substrate. A layer of poly(ethylene glycol) was subsequently applied to the selection of prepared specimens to create a bilayer ceramic/polymer coating. Electrochemical and immersion corrosion tests revealed that the application of a bilayer coating allowed achieving the desired acceleration of degradation, while the application of only a ceramic coating led to a reduction in the corrosion rate. A slight increase in the corrosion rate was observed for samples with bioactive drug-containing coatings compared to samples with drug-free coatings. Higher viability of human fibroblastic cells cultured in the extracts of the tested samples was noted for samples with a bilayer coating compared to a ceramic coating. The addition of gentamicin in the bioactive coatings had no significant effect on the viability value. Antibacterial tests proved the antibacterial activity of samples with a gentamicin-loaded coating layer against *Escherichia coli* and *Staphylococcus aureus* strains. A detailed study of the release of gentamicin from the prepared coatings revealed a different mechanism of drug release from the ceramic and the ceramic/polymer coating. Furthermore, it was found that the drug was released more slowly and uniformly from the bilayer coating. It is therefore possible to adjust the amount and duration of drug release from the bioactive coating by the thickness of the upper polymer layer. Incorporation of an antibiotic in a combined ceramic/polymer coating enabled the creation of a high-performance bioactive coating for Fe bone implants with the possibility to release a drug in the vicinity of the implant in a controlled manner to address the needs of the patient.

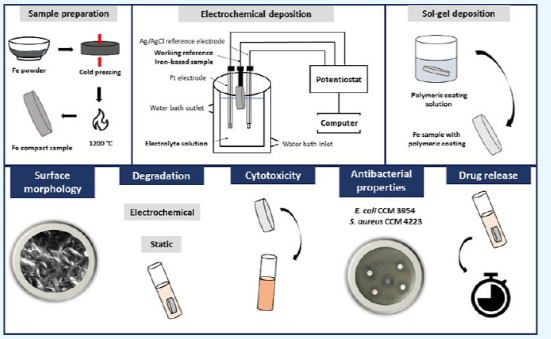


Downloaded via TOMAS BATA UNIV IN ZLIN on January 29, 2025 at 14:52:47 (UTC).
See https://pubs.acs.org/sharingguidelines for options on how to legitimately share published articles.

## 1. INTRODUCTION

The number of patients with fractures requiring surgery increases significantly every year, and the implantation of suitable materials is an effective means of treating these bone defects. Biodegradable materials as implant materials have become a trend in recent years.[1]

As a biodegradable material, iron is considered one of the most suitable biodegradable metals up to today due to its great modulus of elasticity and high strength. Due to the slow-going corrosion and therefore insufficient rate of biodegradation, iron materials are not normally used in practice. Many studies have been published that propose different techniques that can accelerate their corrosion rate of iron biomaterials.[2] The coating of iron materials with bioresorbable polymers brings promising results. During degradation, bioresorbable polymers locally acidify the environment around the implant. For example, studies by Yusop et al. showed that iron corrosion is accelerated by the acidic hydrolysis of PLGA.[3] Qi et al. focused on the behavior of an iron stent coated with polylactic acid. Based on their results, the 50 $\mu$m-thick strut completely

Received: July 4, 2024
Revised: October 24, 2024
Accepted: November 13, 2024
Published: November 27, 2024

© 2024 The Authors. Published by American Chemical Society

dissolved after 6 months.[4] Likewise, the research of Gorejová et al. showed that coating the iron surface with PEI coatings at different concentrations provided the desired increase in corrosion rate mediated by polymer cracking and penetration of the corrosion medium.[5]

Surface modifications of resorbable metallic materials can enhance their biological compatibility by increasing the surface activity of the implant in living tissue as well as the corrosion properties. The surface properties of materials also have an impact on the process of material−tissue integration.[6] One of the most widely used ceramic coatings for improving the biocompatibility of metal surfaces is calcium phosphate (CaP). CaP coatings, such as $Ca_{10}(PO_4)_6(OH)_2$ (hydroxyapatite, HAP) or $CaHPO_4{\cdot}2H_2O$ (brushite), have been quite extensively investigated as a biomaterial for bone implants due to their chemical similarity to the inorganic phase of bone.[7] The biggest advantage is the biocompatibility of the HAP coating, as it has the ability to induce the growth of a new layer of bone apatite in the body environment.[8] Coatings applied to metal implants can be made of pure HAP, HAP doped with drugs, or composite coatings composed mainly of HAP and a polymer, such as chitosan (CS) or poly(ethylene glycol) (PEG). Unmodified HAP is relatively fragile; therefore, its application is limited. A ceramic/polymer multilayer coating improves the mechanical properties of HAP while mimicking the natural composition of bone (HAP and collagen). Since PEG is biocompatible, biodegradable, and nontoxic to the human body, it is a suitable polymer for biomedical use.[9−11]

Coatings on metal materials can be produced using various techniques, such as electrodeposition,[12−15] plasma spray,[16] or sol−gel method.[17] Electrochemical deposition is one of the suitable methods to produce coatings, mainly due to its availability and low cost, as well as the possibility to modify various samples' geometries and the ability to control the homogeneity, composition, and thickness of the coating by controlling either the current or voltage.[18]

In the past decade, focus has been aimed to the improvement of drug delivery devices. The electrochemical deposition technique has been used to produce bioactive coatings doped with various antibiotics, such as ciprofloxacin,[19] vancomycin, or gentamicin.[20,21]

Bone infection leading to various complications (osteonecrosis, amputation or sepsis) can occur during or after surgical procedures.[22] Drug-doped coatings could prevent possible infections with orthopedic implants.

The presented article is focused on the study of the possibilities of preparing ceramic, ceramic/polymer, and bioactive drug-doped coatings onto iron biodegradable samples and the subsequent comparison of the prepared materials in terms of their degradation properties under both static and dynamic conditions, as well as the study of drug release, cytotoxicity, and antibacterial testing.

## 2. MATERIALS AND METHODS

**2.1. Preparation of Iron-Based Materials.** Iron-based specimens were produced from carbonyl iron powder from BASF (CC type, d50 value of 3.8−5.3 $\mu$m) by cold pressing into cylindrical shapes (Ø 12 mm, h 2 mm) at a pressure of 600 MPa. Subsequently, sintering in a tube furnace filled with a reducing atmosphere (hydrogen) at 1120 °C took place for 1 h. Before coating application, all samples were ultrasonically cleaned for 10 min in acetone and 96% ethanol. The cleaning was preceded by treatment of the surface with different grain sandpapers in order to roughen the surface.

**2.2. Electrochemical Deposition of CaP/CaP + Ge Coating.** Preparation of the ceramic CaP layer was carried out by using an Autolab (PGSTAT 302N) potentiostat. The cleaned iron pellet was connected as a working electrode, Ag/AgCl/KCl (3 mol/L) as the reference electrode, and Pt as the auxiliary electrode. The electrolyte solution used for electrolytic deposition of the CaP layer was composed of $2.5 \times 10^{-2}$ mol/L $NH_4H_2PO_4$ and $4.2 \times 10^{-2}$ mol/L $Ca(NO_3)_2$. A current density of 0.85 mA/cm$^2$ was applied during cathodic deposition for the duration of 40 min. Subsequently, the coated samples were immersed in a 1 mol/L NaOH solution at a temperature of 65 °C for 2 h, rinsed with distilled water, and dried at a 80 °C for 2 h (Fe−CaP samples).

The samples coated with a layer of drug-doped CaP were prepared using the same procedure, but gentamicin sulfate (300 mg/50 mL) was added to the electrolyte solution. The coated samples were dried at a temperature of 37 °C for 2 h (Fe−CaP + Ge samples).

**2.3. Sol−Gel Deposition of PEG Coating.** Half of the Fe−CaP and Fe−CaP + Ge samples were modified on the surface with a layer of PEG 4000 (Sigma-Aldrich, USA). The prepared samples were immersed in a 10 wt % PEG ethanol solution for 3 h at laboratory temperature and then dried for the next 3 h at 45 °C (Fe−CaP + PEG and Fe−CaP + Ge + PEG samples).

**2.4. Surface Characterization of the Samples.** Macroscopic images of the surface of the fabricated samples were obtained using an optical digital microscope (Dino-Lite Premier AM4013MT, Distrelec Netherlands) with a resolution of 1.3 MPx and 35× and 150× magnification.

A scanning electron microscope equipped with an energy-dispersive spectrometer (JEOL JSM-7000F, Japan, with EDX INCA) was used to examine the surface morphology of the prepared samples.

Raman spectroscopy was conducted using an XploRA ONE spectrometer (Horiba Yvon Jobin, France) with a 35 mW (original laser power) 785 nm laser source. Spectral data was acquired using a 50× microscope objective over the range of 300−1800 cm$^{-1}$ with a 10 s acquisition time, two accumulations, and 100% laser power.

Fourier transform infrared (FTIR) spectroscopy spectra were obtained by using a Tensor 29 infrared (IR) spectrometer (Bruker, Germany) using the attenuated total reflectance (ATR) technique. The spectra were acquired in the range of 4000−649 cm$^{-1}$.

XRD analysis was done using a Philips (X'Pert Pro) X-ray diffractometer (Bridge Tronic Global, USA) with an X-ray rotating Cu anode operating at 40 kV and 50 mA. The XRD patterns were measured in the angular 2 theta range between 10° and 90° at a time per step of 30 s and a step size of 0.033°.

XPS was done using a Thermo Scientific Nexsa G2 Surface Analysis System (Thermo Fisher Scientific, UK) equipped with a microfocused, monochromatic Al K$\alpha$ X-ray source (1486.68 eV). The survey spectra were collected in constant analyzer energy mode with a pass energy of 200 eV. Narrow spectral areas were captured at a pass energy of 50 eV. Charge compensation was performed by using an Ar flood gun system. Digital collection and data processing were carried out using Thermo Scientific Avantage software, version 6.7.0 (Thermo Fisher Scientific). The surface compositions (in atomic percent) were calculated by taking the integrated peak areas


https://doi.org/10.1021/acsomega.4c06192
ACS Omega 2024, 9, 48299−48314

of the identified atoms and calculating the corresponding sensitivity factor.

**2.5. Degradation of Samples.** *2.5.1. Electrochemical Degradation Test.* The corrosion performance of the prepared samples was observed by the anodic polarization method using an Autolab (PGSTAT 302N, Metrohm, Slovakia) potentiostat with a three-electrode system (coated iron sample as the working electrode, a silver chloride electrode as the reference electrode, and the platinum electrode as the counter electrode). Potentials were changed in the range of ±100 mV from the open-circuit potential (OCP) potential value at a scanning rate of 0.1 mV/s. Tests were performed in Hanks' solution (Table 1) and tempered to 37 ± 2 °C. After the measurement, the samples were rinsed with ethanol and left to dry at room temperature.

**Table 1. Chemical Composition of Hanks' Solution**

| chemical | quantity [g/L] |
|---|---|
| NaCl | 8 |
| KCl | 0.4 |
| $CaCl_2$ | 0.14 |
| $MgSO_4 \cdot 7H_2O$ | 0.1 |
| $MgCl_2 \cdot 6H_2O$ | 0.1 |
| $Na_2HPO_4 \cdot 2H_2O$ | 0.06 |
| Glucose | 1 |
| $KH_2PO_4$ | 0.06 |
| $NaHCO_3$ | 0.35 |

The corrosion rate (CR in mm/year) was calculated using a Tafel extrapolation method according to eq 1 which is based on the ASTM G59 norm[23]

$$\mathrm{CR} = \frac{j_{\mathrm{corr}} \mathrm{KEW}}{d} \quad (1)$$

$j_{corr}$—corrosion current density (A/cm$^2$), $K$—constant determining the resulting units, EW—equivalent weight of studied material, and $d$—material density (g/cm$^3$).

Before the electrochemical degradation tests were started, the OCP was measured for 60 min. The OCP value was utilized in an electrochemical impedance spectroscopy (EIS) measurement which was performed in the frequency range of 10 mHz−100 kHz with an alternating current amplitude of 10 mV.

*2.5.2. Immersion Degradation Test.* Before the beginning of the immersion test, the samples were carefully weighed ($m_i$). The Fe sample was cleaned using an ultrasonic bath in acetone and ethanol for 10 min before the test. The tested samples were immersed into Hanks' solution for 30, 60, and 90 days at a temperature of 37 °C. After the indicated time (30, 60, and 90 days) were samples ultrasonically cleaned in acetone and ethanol (10 min each), air-dried, and finally weighed ($m_f$). The rate of corrosion (CR) was calculated based on the change in the weight according to eq 2 and based on the ASTM G31 norm[24]

$$\mathrm{CR} = \frac{(m_i - m_f)K}{Atd} \quad (2)$$

CR—corrosion rate, $m_f$—final weight of the sample, $m_i$—initial weight of the sample, $K$—constant determining output CR units (87,600), $A$—surface area of the sample, $t$—time of exposure, and $d$—sample density.

**2.6. Cytotoxicity Test.** Cytotoxicity tests were performed in vitro in accordance to standard STN ISO 10993−5.[25] Samples of Fe, Fe−CaP, Fe−CaP + PEG, Fe−CaP + Ge, Fe−CaP + Ge + PEG, and stainless steel (SS) were sterilized by a germicidal lamp and placed in 24-well plates, to which 2 mL of culture medium was added. For 4 and 24 h, the samples were placed in a culture medium made up of Dulbecco's modified Eagle's medium with 10% fetal bovine serum and 1% antibiotic solution (ATB). The samples were then removed from the tubes, and the extracts were centrifuged at 10,000 rpm for 5 min.

The extracts were then utilized to assess their cytotoxicity in vitro. Human dermal fibroblast cells (HDFa; Sigma-Aldrich) were placed into a 96-well plate. The culture medium with the cells was removed from each well, and the cell concentration was determined in a Bürker chamber. $10^4$ HDFa were present in each cell after 100 μL of growth media was supplied to each plate well.

Cells were cultivated until the monolayer was formed, which took place for 24 h in an incubator (temperature of 37 °C, 95% humidity, 5% $CO_2$). After 1 day of incubation was the culture medium pipetted from every single well. Then, the prepared extracts were added to wells with the cells and left to incubate for 4 h. Each experiment was repeated in triplicates for each sample. Wells without extract were used as a negative control (NC).

After cultivation, the in vitro cytotoxicity of the extracts was determined using the MTS proliferation test (CellTiter 96 AQueous one solution cell proliferation assay, Promega, USA). After that, 100 μL of MTS reagent was added to each plate well and incubated for 4 h at 37 °C. After determining the formazan's absorbance at 490 nm with a UV−vis spectrophotometer (Shimadzu), cell viability was computed using eq 3

$$V(\%) = \frac{\mathrm{OD}}{\mathrm{OD}_{\mathrm{NC}}} \times 100\% \quad (3)$$

OD—optical densities of the iron samples tested and $OD_{NC}$—optical density of the NC test.

**2.7. Antibacterial Activity.** Bacterial strains *Staphylococcus aureus* CCM 4223 and *Escherichia coli* CCM 3954 (Czech Collection of Microorganisms, Brno) were used to test the antibacterial activity of CaP and CaP + Ge by the qualitative disk-diffusion method according to standard ISO 20645−2004.[26] From the 18 h culture of the tested strains, a suspension was prepared in a sterile physiological solution adjusted to a value of 0.5 on the McFarland scale. The prepared suspensions were inoculated on Mueller−Hinton agar in a volume of 100, and 10 μL of CaP and CaP + Ge in the concentration range of gentamicin from 6 to 0.75 mg/mL was pipetted onto paper disks with a diameter of 6 mm. Nutrient media were cultured for 1 day at 37 °C. The diameter of the zone of growth inhibition was measured in millimeters to assess the antibacterial activity. As a control, an antibiotic disc with gentamicin (10 μg) was ingested.

**2.8. Gentamicin Release.** *2.8.1. EIS and Conductivity Measurements.* EIS (Solartron Analytical Modulab) and conductivity measurements (WTW Inolab Level 1) were used to evaluate the release of gentamicin from the CaP + Ge and CaP + Ge + PEG coatings. EIS measurements were performed from a 100 kHz to 1 Hz frequency range with a 10 mV amplitude at a potential of 15 mV (vs the reference electrode) in PBS solution. Data from the EIS measurements were evaluated by using the ZView program.



https://doi.org/10.1021/acsomega.4c06192
ACS Omega 2024, 9, 48299−48314

The presence of gentamicin sulfate in the solution caused an increase in the conductivity when dissolved in pure water. Thus, from changes in the conductivity of the solution due to the release of gentamicin from the coating, its concentration was calculated using a calibration curve. Distilled water was used for conductivity measurements to avoid the contribution of Hanks' solution components.

**2.9. UV−Vis Spectroscopy Measurements.** Determination of the gentamicin release from the compact Fe−CaP + Ge and Fe−CaP + Ge + PEG samples was also carried out by using UV−vis spectrometry. Prepared coatings containing gentamicin were placed in 10 mL of PBS at pH 7.4 for 48 h at 37 °C. After 1, 2, 4, 6, 8, 12, 24, and 48 h, 0.9 mL of the dissolution medium was pipetted out, and the same volume of fresh PBS was added.

Standard solutions with gentamicin concentrations ranging from 2 to 10 mg/mL were used to create a calibration curve. The drug release data were kinetically analyzed using Kinet DS3 software according to various kinetic models. Linear regression equations were used, based on which the regression coefficient of determination ($R^2$) was obtained.[27]

The individual parameters and the regression coefficient were calculated based on the following equations (eqs 4−7) for the individual models

$$\text{Korsmeyer} - \text{Peppas model: } Q = k{\cdot}t^n \quad (4)$$

**Table 2. Types of the Release Mechanism Depending on the Exponent $n$[28]**

| diffusion exponent $n$ | diffusion mechanism |
|---|---|
| 0.45 | classical Fick diffusion |
| 0.45 < $n$ < 0.89 | anomalous ("non-Fick") transport, manifest both ways: diffusion and relaxation/erosion of the polymer |
| 0.89 | "case-II" relaxation transport, release of zero order with simultaneous erosion of the polymer |
| $n$ > 0.89 | "super case-II" transport |

the value of the release exponent $n$ characterizes different release mechanisms. Table 2 lists the types of release mechanism depending on the value of the exponent $n$.

$$\text{Higuchi model: } Q = k{\cdot}\sqrt{t} \quad (5)$$

$$\text{Zero} - \text{order model: } Q = k{\cdot}t + Q_0 \quad (6)$$

$$\text{First} - \text{order model: } \frac{1}{Q} = k{\cdot}t + \frac{1}{Q_0} \quad (7)$$

where $Q$ = amount of drug released at time $t$, $Q_0$ = initial value of Q, $k$ = constant, and $t$ = time.

## 3. RESULTS AND DISCUSSION

**3.1. Surface Morphology and Composition.** The weight of the coating deposited onto the surface of the iron samples was determined from the weight difference after and before coating layer deposition. The weight of the CaP and CaP + Ge coating layer was about 1.06 and 1.33 mg/cm$^2$, respectively. The weight of the PEG layer in the CaP + PEG and CaP + Ge + PEG samples was ∼2.1 mg/cm$^2$. The deposited coating layers were adhered and stable.

Several techniques were used to examine the prepared materials' surface morphology. Macroscopic images of the as-prepared materials obtained by optical microscopy are shown in Figure 1. Scratches were visible on the surface of the uncoated Fe sample (Figure 1a) due to the roughening of the sample surface by abrasive papers. After the deposition of the ceramic CaP layer (Figure 1b), star-shaped microstructures were observed, which were also present on the surface of the drug-doped CaP coating (CaP + Ge, Figure 1d). The deposition of a polymer PEG layer on the surface of the ceramic coating (Figure 1c,e) resulted in smoothing of the surface of the samples.

SEM analysis of the surface of the coated samples showed the existence of uneven ceramic coatings obtained by electrochemical deposition on the surface of the Fe−CaP and Fe−CaP + Ge samples (Figure 2b,d) and confirmed the presence of a polymer coating layer obtained by the sol−gel method on the surface of the Fe−CaP + PEG and Fe−CaP + Ge + PEG samples (Figure 2c,e). The microstructures of different sizes composed of thin plates and dendrites, in addition to irregularly dispersed rod-shaped microstructures, were observed on the surface of the ceramic-coated samples (CaP and CaP + Ge) (Figure 2b,d).

After the deposition of the polymer layer, the microstructures observed in the ceramic coating were covered, and the surface of the Fe−CaP + PEG and Fe−CaP + Ge + PEG samples was smoothed (Figure 2c,e).

The presence of the coating and its thickness were investigated using cross-sectional SEM images. Figure 3 displays the cross-sectional SEM images of the prepared iron-based material before and after coating with CaP and CaP + PEG, respectively. As shown in Figure 3b, a thin discontinuous CaP coating layer was deposited on the Fe substrate, and its thickness is approximately 500 to 1000 nm. After applying the PEG coating on the Fe−CaP sample, the bilayer coating with a thickness from 200 to 700 nm was formed (Figure 3c).

The presence of both the ceramic and polymer coating layers on the surface of the samples was proven by EDX analysis. The average surface composition of the prepared samples is shown in Table 3. The ceramic coating location on the surface of all samples was confirmed based on the presence of calcium and/or phosphorus contained in the CaP layer, and the existence of a polymer coating on the surface of the Fe−CaP + PEG and Fe−CaP + Ge + PEG samples was confirmed by the presence of oxygen and carbon, originating from the PEG layer, in the EDX spectra of these samples. Neither of these elements was observed in the EDX spectrum of the uncoated Fe sample.

The presence of gentamicin sulfate in the coating was confirmed by the presence of sulfur in the Fe−CaP + Ge and Fe−CaP + Ge + PEG samples, which was not observed in the spectra of the other samples.

A more accurate distribution of the basic elements can be seen in the distribution maps obtained by the surface EDX analysis of the sample surfaces shown in Figure 4, where a uniform distribution of the elements on the surface of the prepared samples can be observed.

Figure 5a demonstrates the XRD analysis results of the prepared samples. As is apparent from all diffractograms, the Fe substrate (card no. 87-0722) was represented by three typical peaks observed at 44.7°, 65.1°, and 82.3° 2 theta. As further shown, a low-intensity peak of nanocrystalline


https://doi.org/10.1021/acsomega.4c06192
ACS Omega 2024, 9, 48299−48314

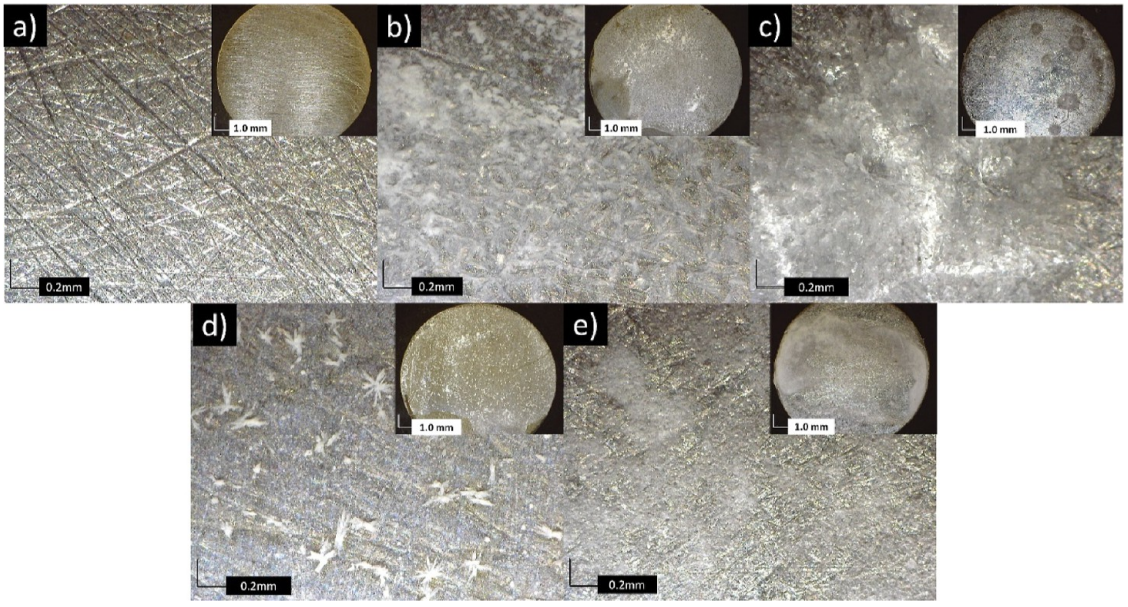


**Figure 1.** Optical microscopy images of the surface of studied samples: (a) Fe, (b) Fe−CaP, (c) Fe−CaP + PEG, (d) Fe−CaP + Ge, and © Fe−CaP + Ge + PEG samples (magnification 35× and 150×).

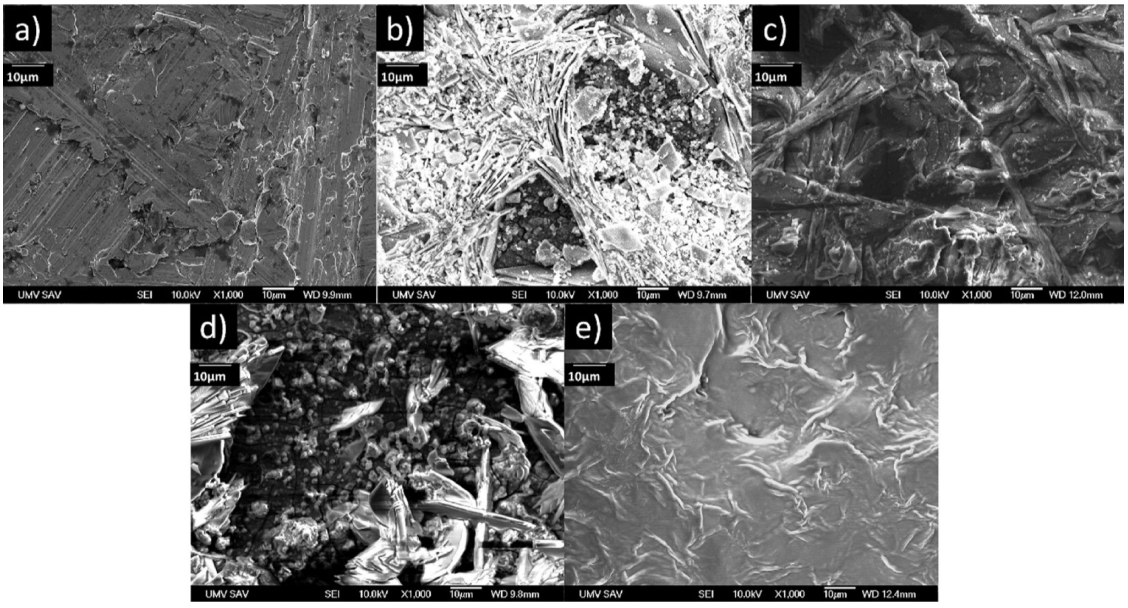


**Figure 2.** SEM micrographs of the surface of studied samples: (a) Fe, (b) Fe−CaP, (c) Fe−CaP + PEG, (d) Fe−CaP + Ge, and (e) Fe−CaP + Ge + PEG samples (magnification 1000×).

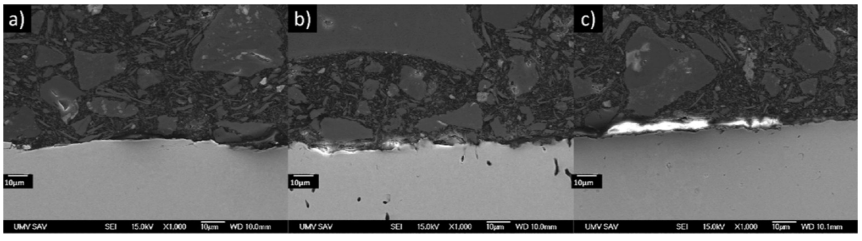


**Figure 3.** Cross-sectional SEM images of studied (a) Fe, (b) Fe−CaP, and (c) Fe−CaP + PEG samples (magnification 1000×).

hydroxyapatite at ∼26° and ∼33° 2 theta (card no. 24-0033) was detected in all the CaP-coated samples (Fe + CaP, Fe + CaP + PEG, and Fe + CaP + Ge + PEG), except for the Fe + CaP + Ge sample. The sample coated with the gentamicin-doped CaP coating (Fe + CaP + Ge) showed no reflections originating from hydroxyapatite, but instead, a brushite phase (card no. 02-0085) was found in the XRD pattern with a typical strong reflection observed at 11.6°, 20.9°, and 29.2° 2



https://doi.org/10.1021/acsomega.4c06192
ACS Omega 2024, 9, 48299−48314

Table 3. Surface Composition of Prepared Samples Determined by EDX Analysis

| sample | surface chemical composition (wt %) | | | | | | | |
|---|---|---|---|---|---|---|---|---|
| | Fe | C | O | Na | P | Ca | S | N |
| Fe | 100 | | | | | | | |
| Fe−CaP | 5.00 | 6.80 | 3.65 | 1.46 | 16.26 | 34.19 | | |
| Fe−CaP+Ge | | 9.99 | 47.74 | | 16.83 | 23.64 | 1.79 | |
| Fe−CaP+PEG | 1.02 | 42.70 | 34.58 | 1.30 | 8.60 | 11.80 | | |
| Fe−CaP+Ge+PEG | 0.94 | 53.03 | 31.75 | | 0.05 | | 0.08 | 14.27 |

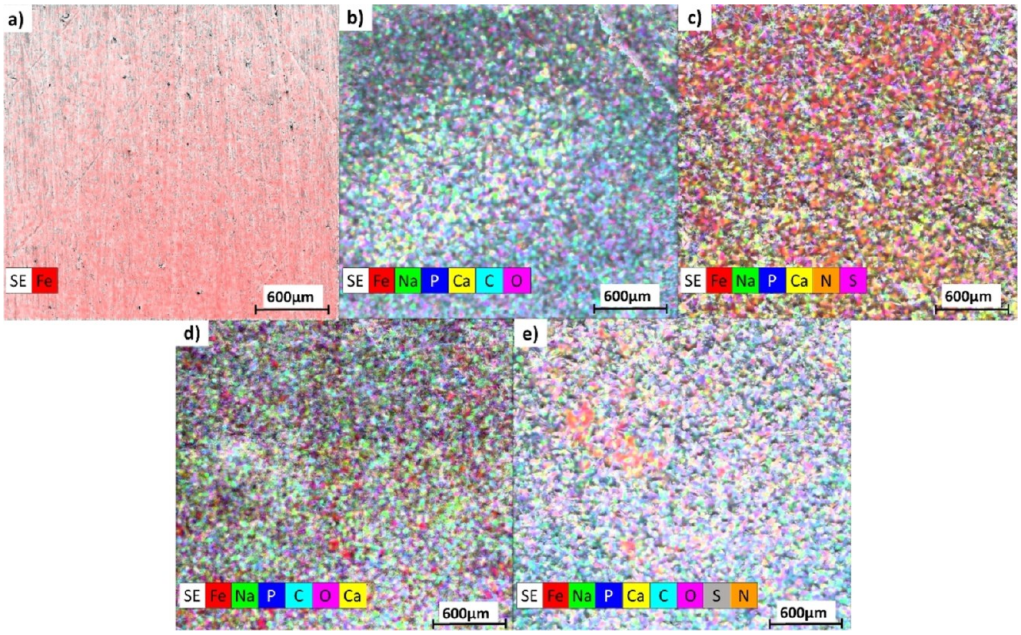


**Figure 4.** Energy-dispersive X-ray (EDX) mapping analysis of (a) Fe, (b) Fe−CaP, (c) Fe−CaP + Ge, (d) Fe−CaP + PEG, and (e) Fe−CaP + Ge + PEG samples.

theta, respectively. The formation of the brushite phase was probably due to the acidic environment caused by gentamicin sulfate, while the PEG polymer in the Fe + CaP + Ge + PEG sample buffered the pH toward a more neutral pH, causing the formation of a thermodynamically more stable HAP phase.

Figure 5b displays the produced materials' FTIR spectra. Pure iron is free from any IR bands. After the introduction of CaP, two signals located at 1000−1100 and 1460−1500 $cm^{-1}$ occurred. The former is due to the triply degenerated $\nu_3PO_4$ asymmetric mode (with the shoulder peak on the left) of the CaP.[29,30] The introduction of gentamicin did not result in a change of the FTIR spectra as its concentration was low. On the contrary, after the addition of PEG, many intensive bands appeared. The two most intensive ones, located at 2881 and 1109 $cm^{-1}$, correspond to the stretching vibrations of the C−H group and the C═O group in PEG, respectively.[31,32] The IR bands corresponding to CaP can no longer be observed, as those originating from PEG are much more intensive.

The Raman spectra recorded for all prepared samples are shown in Figure 5c. The characteristic peaks corresponding to the literature survey[33−35] are clearly visible in case of pure Ge, PEG, and CaP, while pure Fe has no Raman peaks. The sample coated with CaP shows a small peak at 964 $cm^{-1}$, which contributes to the totally symmetric $(PO_4)^{3-}$ stretching mode of the "free" tetrahedral phosphate ion.[34] After the addition of gentamicin to the coating, the same peak was observed but with very low intensities, indicating the presence of brushite in the coating. After the coating of the Fe−CaP sample with PEG, the peaks of both CaP and PEG are presented in the Raman spectrum, which indicates a nonhomogeneous coating layer of PEG. Finally, the Fe−CaP−Ge−PEG sample only shows peaks of PEG, from which it can be concluded that the surface of the sample was continuously covered with a layer of PEG.

To further investigate the chemical condition of the elements present at the sample's surface, XPS analysis was carried out (Figure 5d, Table 4). The Fe substrate showed considerable oxidation on the surface, and mainly $Fe^{3+}$ (Fe $2p_{3/2}$ at ∼710.6 eV) species are present on the surface (Table 4). Some surface contamination by mostly organic (high carbon content) species also containing nitrogen and inorganic cation $Ca^{2+}$ (Ca 2p at ∼348 eV) was also detected. After CaP deposition, the signal of the Fe substrate almost disappeared (only 0.1 atom % of Fe present), and the peaks typical for CaP were clearly detected (Ca 2p at ∼348 eV representing $Ca^{2+}$ and P 2p at ∼134 eV representing $PO_4^{3-}$). No nitrogen was present in the case of the Fe−CaP sample. After the introduction of Ge, a small amount of N 1s was present at about 400 eV, representing $-NH_2$ (Table 4). However, CaP signals dominate the Fe−CaP−Ge sample surface. After PEG was added to the surface, only signals related to the PEG structure were visible. This was represented by a strong C−O signal typical of PEG, C 1s at ∼286.4 eV and O 1s at ∼532.8 eV (Table 4).[36]

**3.2. Degradation Behavior.** *3.2.1. Electrochemical Degradation Behavior.* The OCP was measured for 1 h prior to further measurements. OCP values stabilized in the range from


https://doi.org/10.1021/acsomega.4c06192
ACS Omega 2024, 9, 48299−48314

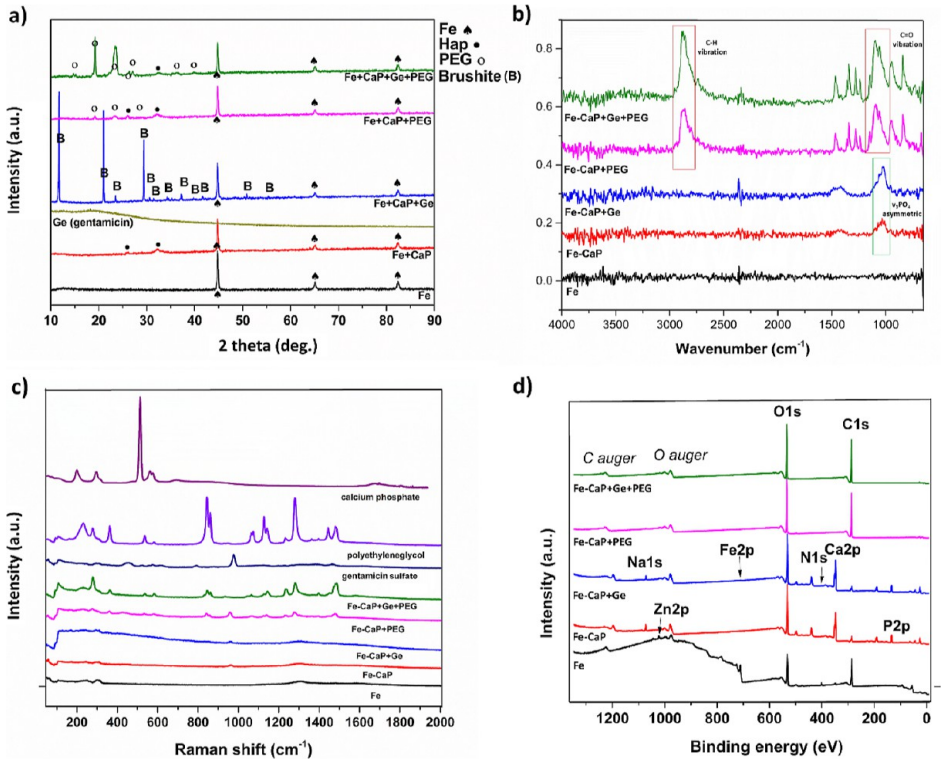


**Figure 5.** (a) XRD spectra, (b) IR spectra, (c) Raman spectra of Fe, Fe−CaP, Fe−CaP + PEG, Fe−CaP + Ge, and Fe−CaP + Ge + PEG samples, and (d) XPS spectrum survey of the prepared Fe, Fe−CaP, Fe−CaP + Ge, Fe-Cap + Ge, and Fe−CaP + Ge + PEG sample.

**Table 4. Apparent Surface Chemical Composition as Assessed by XPS**

| sample | chemical composition of samples' surfaces (at.%) | | | | | |
|---|---|---|---|---|---|---|
| | C 1s (C−O) | O 1s | Fe 2p $Fe^0/Fe^{3+}$ | Ca 2p | P 2p | N 1s/Na 1s/Zn 2p/Cl 2p |
| Fe | 55.7 (8.4) | 32.4 | 5.6<br>1.2/4.4 | 0.7 | | 3.6/——/1.3/0.8 |
| Fe−CaP | 15.6 (2.7) | 53.0 | 0.1<br>—/0.1 | 15.6 | 12.4 | ——/3.3/—/— |
| Fe−CaP + Ge | 16.7 (0.6) | 54.1 | 0.1<br>—/0.1 | 16.3 | 10.4 | 0.5/1.8/—/— |
| Fe−CaP + PEG | 67.6 (42.3) | 32.4 | | | | —/—/—/— |
| Fe−CaP + Ge + PEG | 66.9 (42.0) | 33.1 | | | | —/—/—/— |

−0.42 to −0.63 V for each sample around 30 min of measurement (Figure 6a). The lowest OCP values were spotted for the Fe−CaP and Fe−CaP + Ge samples. This observation may indicate the lowest corrosion tendency for the ceramic-coated samples. The highest OCP values were observed for polymer-coated Fe−CaP + PEG and Fe−CaP + Ge + PEG samples, indicating the highest tendency to corrosion among the studied samples. The dynamic polarization tests were performed in body-simulating Hanks' solution at the physiological temperature of 37 °C to determine the corrosion rate (CR).

Table 5 shows the values of electrochemical parameters such as corrosion potential ($E_{corr}$), corrosion current density ($j_{corr}$), and CR values determined by the Tafel extrapolation method from the potentiodynamic polarization curves (Figure 6b).

A potential shift to more positive values was observed for samples with the CaP coating and the gentamicin-doped CaP coating. This indicates higher corrosion resistance compared to that of uncoated Fe samples. The gentamicin-doped CaP coating sample showed a modest change to a more negative potential value when compared with the Fe−CaP sample. This may suggest that the addition of an antibiotic improves the materials' corrosion properties.

The corrosion rate values (Table 5) calculated according to eq 1 showed that the addition of the polymer coating caused an increase in the degradation rate compared with pure Fe and also to the CaP-coated samples. The PEG-coated samples (Fe−CaP + PEG and Fe−CaP + Ge + PEG) corroded more than 1.5 times faster than the uncoated Fe sample and more than 2 times faster than the ceramic-coated samples. The greatest corrosion rate was observed for the Fe−CaP + Ge + PEG sample (0.8553 mm. $year^{-1}$).

This result is in line with the trend observed for corrosion potential values and indicates a higher thermodynamic tendency of the polymer-coated samples to corrosion. The obtained potentiodynamic curves for the individual samples are shown in Figure 6b.

The accelerated corrosion of PEG-coated samples is linked to localized acidity near the surface, which originates from the oxidative degradation of PEG.[37−40] A decrease in pH increases


https://doi.org/10.1021/acsomega.4c06192
ACS Omega 2024, 9, 48299−48314

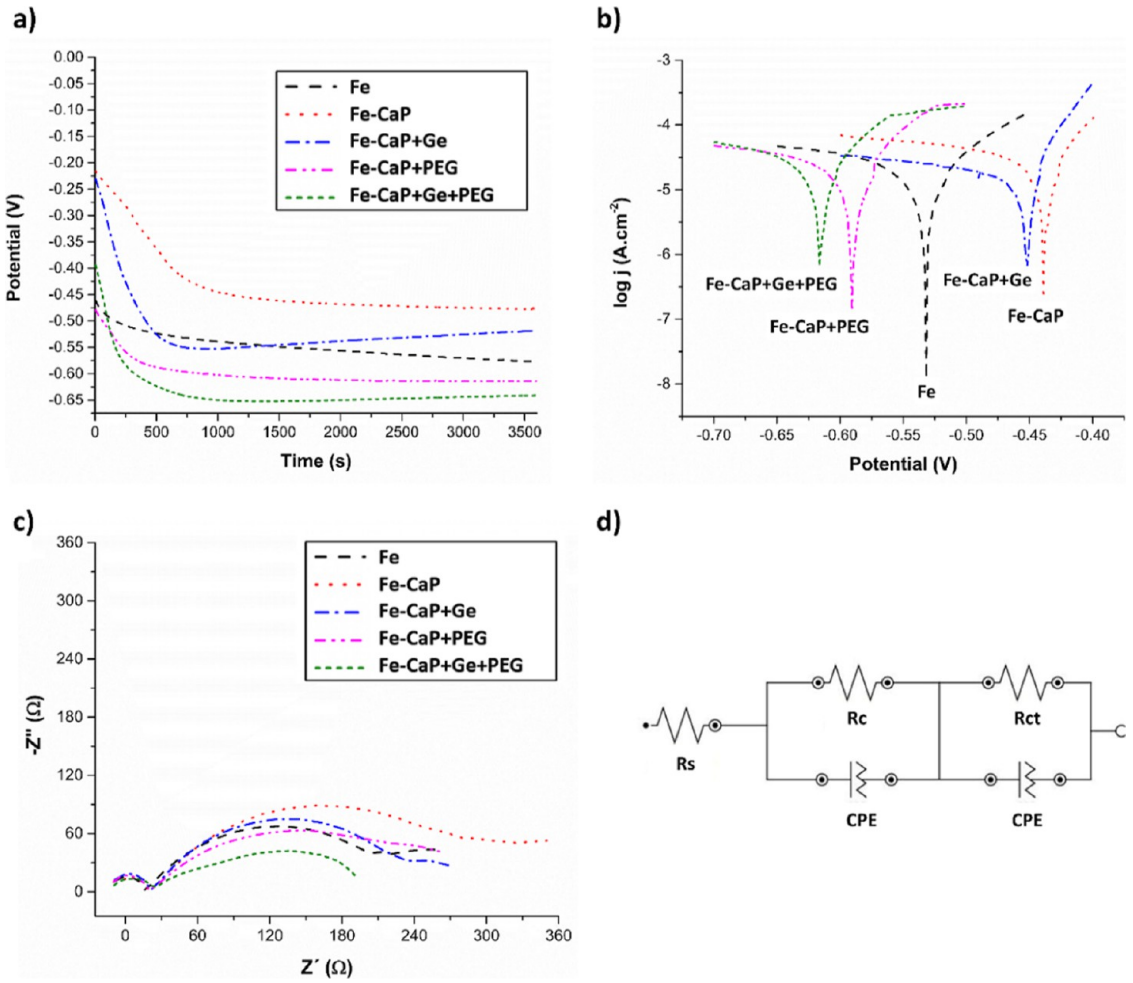


**Figure 6.** (a) OCP curves of samples before degradation in Hanks' solution. (b) Potentiodynamic curves of samples after degradation in Hanks' solution. (c) Nyquist diagrams of Fe, Fe−CaP, Fe−CaP + PEG, Fe−CaP + Ge, and Fe−CaP + Ge + PEG samples in Hanks' solution. (d) Equivalent circuit.

**Table 5. Values of $E_{corr}$, $J_{corr}$, and CR of Prepared Samples after the Degradation Test**

| | $E_{corr}$ (V) | $j_{corr}$ ($\mu$A/cm$^2$) | CR (mmpy) |
|---|---|---|---|
| Fe | −0.5317 | 45.0740 | 0.5237 |
| Fe−CaP | −0.4380 | 29.7170 | 0.3470 |
| Fe−CaP + Ge | −0.4530 | 31.3130 | 0.3638 |
| Fe−CaP + PEG | −0.5910 | 64.3920 | 0.7482 |
| Fe−CaP + Ge + PEG | −0.6153 | 73.6110 | 0.8553 |

**Table 6. Values of the $R_{ct}$ Parameter**

| sample | $R_{ct}$ (Ω) |
|---|---|
| Fe | 282.06 |
| Fe−CaP | 338.10 |
| Fe−CaP + Ge | 311.94 |
| Fe−CaP + PEG | 244.92 |
| Fe−CaP + Ge + PEG | 244.81 |

the solubility of corrosion products, preventing their precipitation and allowing for greater oxygen diffusion. Additionally, the acidic environment promotes proton reduction at the cathode, leading to an increase in corrosion current density and, consequently, higher corrosion rates.

The results of EIS analysis of the prepared samples in Hanks' solution are shown in Figure 6c as Nyquist plots. The diameters of the semicircles for the uncoated Fe sample as well as for the samples coated with CaP and CaP doped with gentamicin are larger than those for the samples with PEG coating (Fe−CaP + PEG and Fe−CaP + Ge + PEG), indicating a higher corrosion susceptibility of the polymer-coated samples.

Figure 6d shows the equivalent circuit used to model the Nyquist diagrams of the Fe, Fe−CaP, Fe−CaP + Ge, Fe−CaP + PEG, and Fe−CaP + Ge + PEG samples. In this circuit, $R_s$ stands for the solution resistance, $R_c$ for the ceramic/polymer layer resistance, $R_{ct}$ for the charge transfer resistance, and CPE are elements of a constant phase. The $R_{ct}$ values for all coated and uncoated samples were calculated as the difference in impedance at lower and higher frequencies (Table 6). The observed values for ceramic/polymeric coated samples as well as for gentamicin containing ceramic/polymeric samples were lower than those for uncoated samples and samples without the polymer layer, which shows the same trend as observed from the potentiodynamic polarization measurements. Lower $R_{ct}$ values obtained for the polymer-coated samples (Fe−CaP + PEG and Fe−CaP + Ge + PEG) indicate the desired higher corrosion rate compared to the uncoated Fe samples and coated Fe−CaP and Fe−CaP + Ge samples.

*3.2.2. Immersion Degradation Behavior.* The rate of degradation was also determined using the static immersion



https://doi.org/10.1021/acsomega.4c06192
ACS Omega 2024, 9, 48299−48314

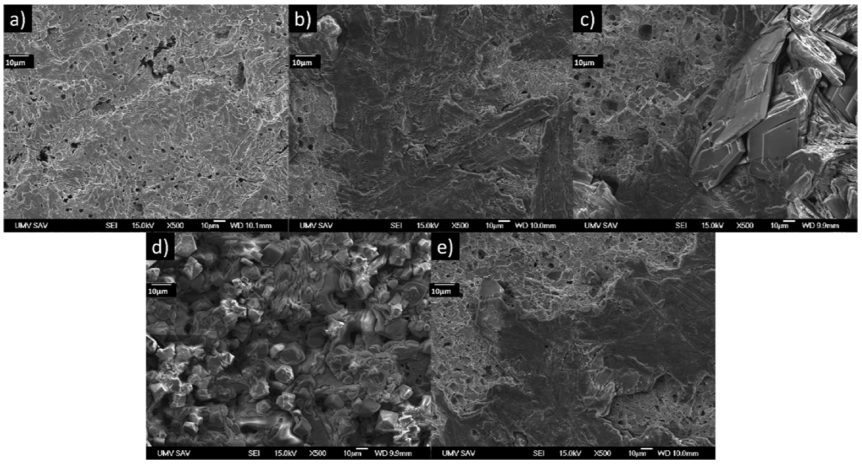


**Figure 7.** SEM micrographs of (a) Fe, (b) Fe−CaP, (c) Fe−CaP + Ge, (d) Fe−CaP + PEG, and (e) Fe−CaP + Ge + PEG samples after immersion in Hanks' solution for 90 days (magnification 500×).

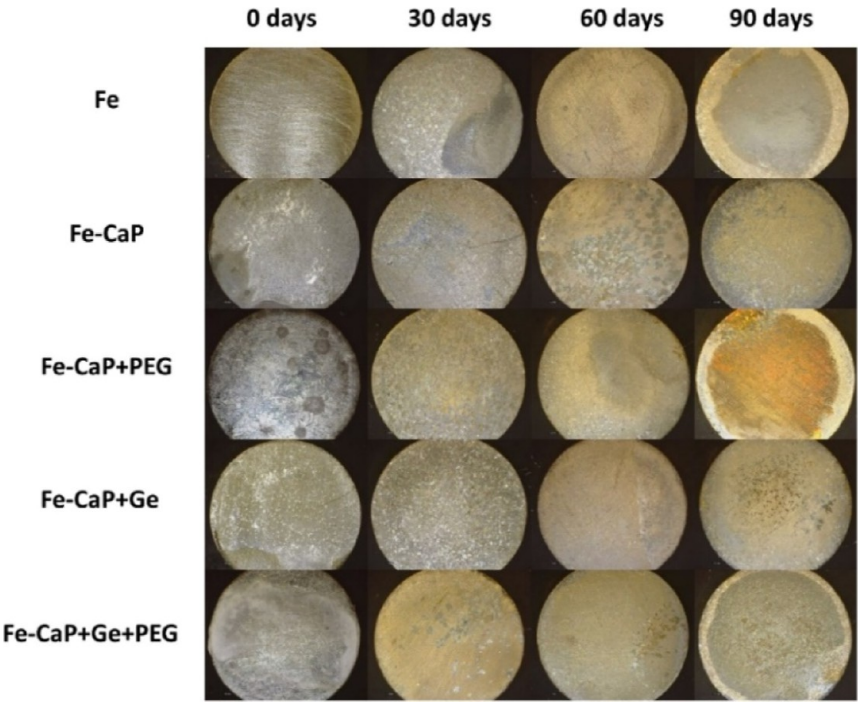


**Figure 8.** Optical images of Fe, Fe−CaP, Fe−CaP + PEG, Fe−CaP + Ge, and Fe−CaP + Ge + PEG samples before and after degradation in Hanks' solution for 30, 60, and 90 days (magnification 35×).

**Table 7. Calculated Corrosion Rate after the Static Degradation Test**

| | CR (mmpy) | | |
|---|---|---|---|
| sample/days of immersion | 30 | 60 | 90 |
| Fe | 0.0447 | 0.0743 | 0.0373 |
| Fe−CaP | 0.0459 | 0.0598 | 0.0332 |
| Fe−CaP + PEG | 0.0453 | 0.0610 | 0.0381 |
| Fe−CaP + Ge | 0.0658 | 0.0792 | 0.0439 |
| Fe−CaP + Ge + PEG | 0.0979 | 0.0870 | 0.0549 |

method. The specimens were immersed in Hanks' solution for 90 days at a temperature of 37 C. The macroscopic pictures of the samples before degradation and after degradation for 30, 60, and 90 days are shown in Figure 8. After 30 days of continuous immersion corrosion testing, uncorroded areas were still observed on the surfaces of all of the samples. There was a more noticeable layer of brown and orange corrosion products on the surface of Fe−CaP + PEG and Fe−CaP + Ge + PEG samples compared to the Fe, Fe−CaP, and Fe−CaP + Ge samples (Figure 8).

After 90 days of corrosion, a layer of corrosion products covered nearly the entire surface of the samples.

The surface morphologies of the samples after immersion tests after 90 days of immersion in Hanks' solution are shown in the SEM images in Figure 7. The microstructure of the Fe sample after corrosion consisted of pits of irregular sizes, as shown in Figure 7a. The samples with the CaP coating retained a relatively intact structure after the immersion test (Figure 7b).

In the samples with CaP + Ge coating, micropores were observed in the microstructure, and their surface was covered



https://doi.org/10.1021/acsomega.4c06192
ACS Omega 2024, 9, 48299−48314

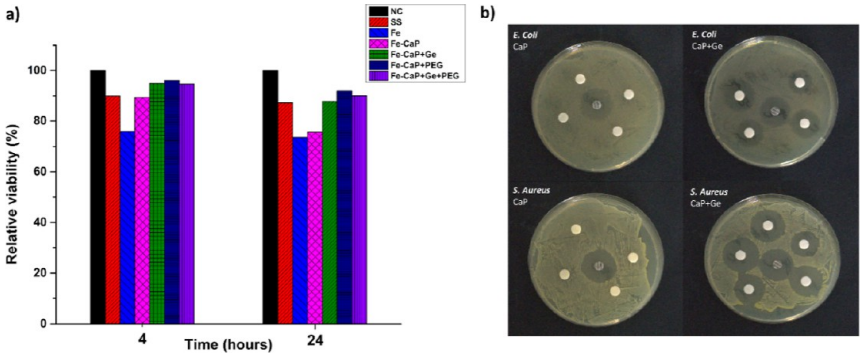


**Figure 9.** (a) HDFa cell relative viability gathered from the MTS assay after cultivation for 4 and 24 h in extraction mediums Fe, Fe−CaP, Fe−CaP + Ge, Fe−CaP + PEG, and Fe−CaP + Ge + PEG samples, stainless steel sheet (SS), and a NC and (b) antibacterial activities of the CaP and CaP + Ge coating against *E. coli* CCM 3954 and *S. aureus* CCM 4223.

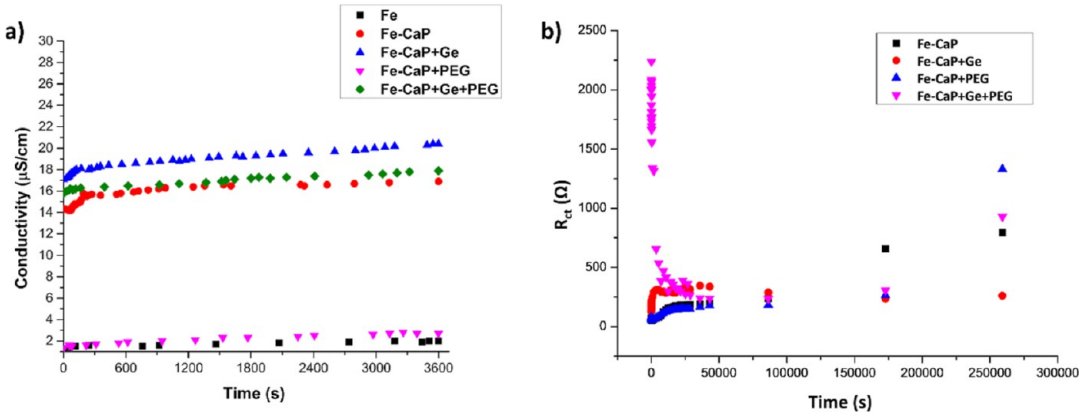


**Figure 10.** (a) Conductivity of Fe, Fe−CaP, Fe−CaP + PEG, Fe−CaP + Ge, and Fe−CaP + Ge + PEG samples and (b) charge transfer-resistant dependence on the time for Fe−CaP (black), Fe−CaP + Ge (red), Fe−CaP + PEG (blue), and Fe−CaP + Ge + PEG (pink) samples for 72 h.

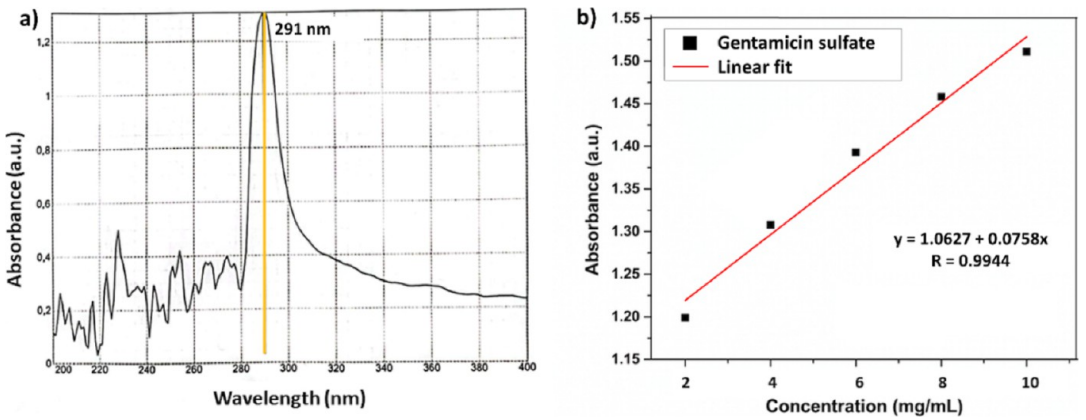


**Figure 11.** (a) UV−vis spectrum of gentamicin sulfate and (b) standard analytical curve of gentamicin sulfate.

by a layer of corrosion products (Figure 7c). SEM images show a higher extent of corrosion for the samples with polymer PEG coating (Figure 7d,e), with a cracked layer of corrosion products. While uniform corrosion was observed for uncoated Fe samples (Figure 7a), aggregates of corrosion products can be seen on the surface of coated samples.

The weight loss upon immersion in Hanks' solution was used to calculate the examined samples' rate of degradation (Table 7). After 12 weeks of immersion, the degradation rate of the uncoated Fe sample was 0.0373 mm/year; the corrosion rate of Fe−CaP and Fe−CaP + Ge samples was 0.0332 and 0.0439 mm/year, and the degradation rate of Fe−CaP + PEG and Fe−CaP + Ge + PEG samples was 0.0381 and 0.0549 mm/year.

These results confirmed the required acceleration of corrosion due to the influence of the polymer coating. The Fe−CaP + Ge + PEG sample lost the most weight after 30 days of immersion in Hanks' solution samples with bilayer CaP and PEG coating, showing slightly higher corrosion rate values compared to uncoated samples and samples with ceramic CaP coating. The disturbed layer of degradation products due to the increased acidity after the dissolution of the PEG coating plays a crucial role in increasing the corrosion rate. A pH drop near the surface of PEG-coated samples leads to the creation of


https://doi.org/10.1021/acsomega.4c06192
ACS Omega 2024, 9, 48299−48314

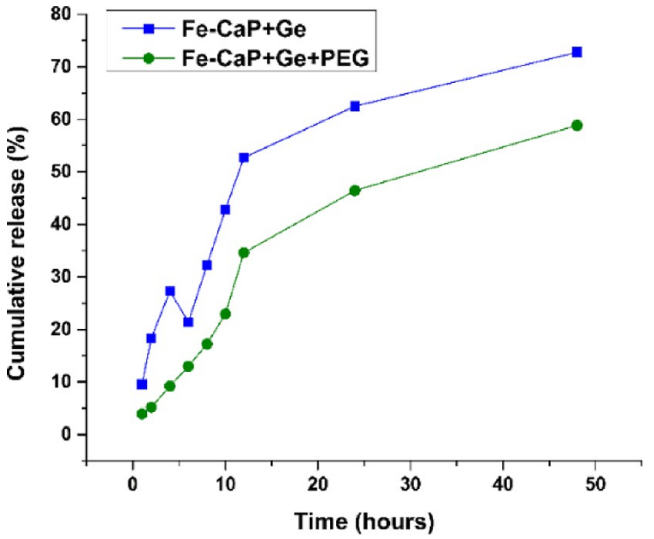


**Figure 12.** Gentamicin release from coatings in PBS (pH 7.4) at 37 °C.

a porous layer of corrosion products, which allows corrosion to continue and does not act passivatingly, as in the case of CaP-coated or uncoated Fe samples.[38,41]

**3.3. Cytotoxicity Test.** The MTS assay was used to study the cytotoxicity of the prepared samples. Figure 9a depicts the viability of HDFa cells cultured in the extraction media for 4 and 24 h. A decrease in cell viability was observed for all extracts compared with the NC.

HDFa cells cultured in the extracts of the Fe−CaP + PEG sample exhibited the highest viability among the tested samples, while cells cultured in the extracts of the uncoated Fe sample had the lowest viability after 4 h of incubation. The Fe−CaP + PEG sample showed very low cytotoxicity with 94.95% cell viability. The viability of HDFa cells in the extracts of Fe−CaP, Fe−CaP + Ge, and Fe−CaP + Ge + PEG samples was 89.25%, 94.95%, and 94.72%, respectively. The presence of a ceramic or polymer coating layer has a positive impact on the viability of HDFa cells and promoted cell proliferation. As the incubation time increased, the cell viability decreased.

Compared with the uncoated iron sample, all the coated samples showed better cell viability. In the case of samples with CaP coating, there was an increase in viability compared to the Fe sample, although better results were observed in the case of bilayer coating in Fe−CaP + PEG and Fe−CaP + Ge + PEG samples. Ceramic-based coatings are known to show no cytotoxic effects but show excellent biocompatibility with hard tissues, skin, and muscle tissues. CaP spontaneously forms a bioactive bone apatite layer on its surfaces in vivo,[42,43] which

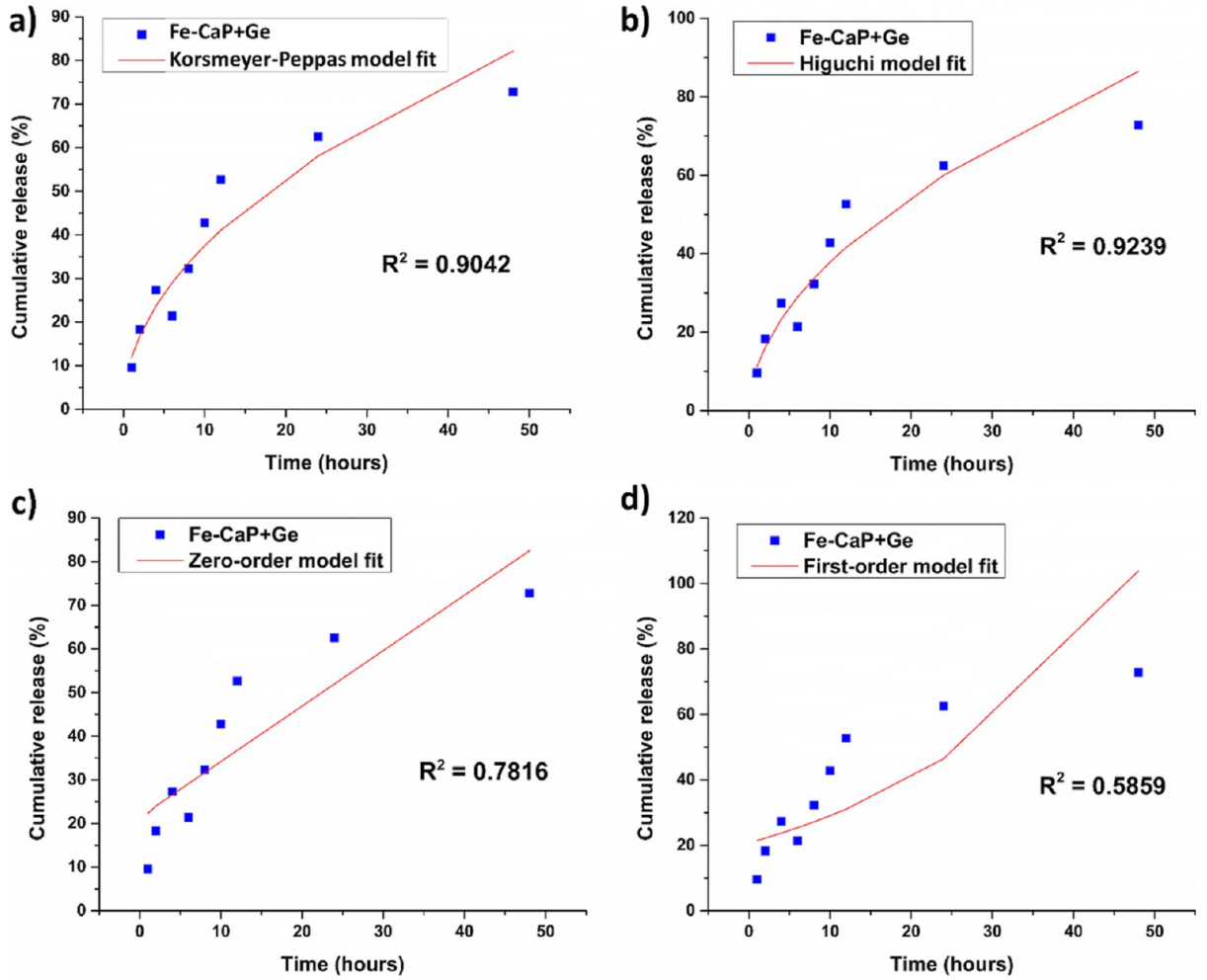


**Figure 13.** Obtained data on drug release from a CaP + Ge coating fitted for different kinetic models: (a) Korsmeyer−Peppas model, (b) Higuchi model, (c) zero-order model, and (d) first-order model.



https://doi.org/10.1021/acsomega.4c06192
ACS Omega 2024, 9, 48299−48314

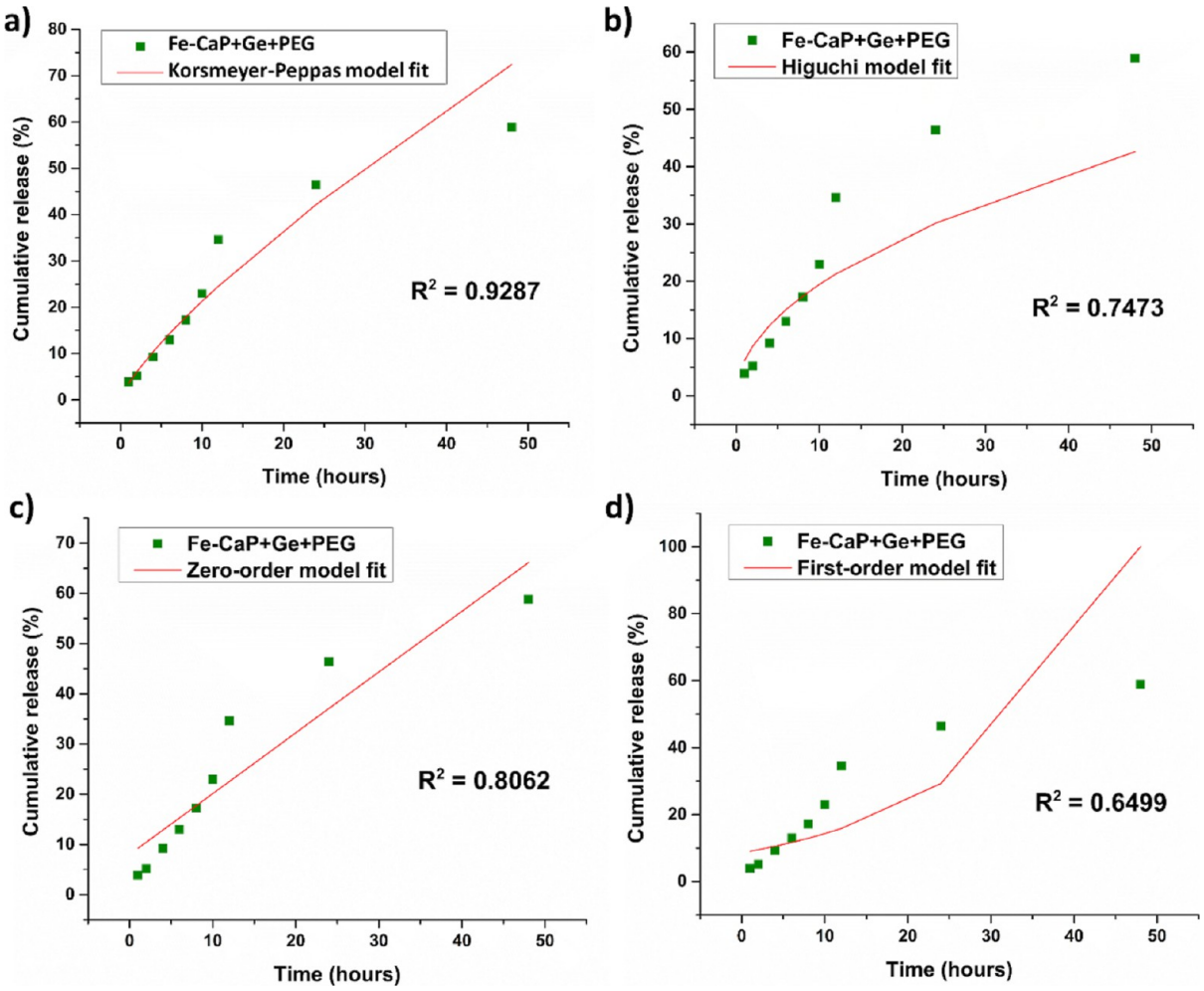


**Figure 14.** Obtained data on drug release from a CaP + Ge + PEG coating fitted for different kinetic models: (a) Korsmeyer−Peppas model, (b) Higuchi model, (c) zero-order model, and (d) first-order model.

acts as an interface between the implant and the tissue.[44] In this work, the beneficial properties of ceramic and polymer coatings were merged to enhance the corrosion properties and biocompatibility of Fe-based biomaterials. Therefore, a polymeric PEG coating was applied to the surface of the samples, which, in addition to improving the degradation properties, also positively affects the cytotoxicity. Based on the viability results, the bilayer coatings showed better results and higher viability of human fibroblastic cells cultured in the extracts of the tested samples compared to the ceramic-coated samples.

After 24 h of cultivation, a decrease in cell viability (below the 90%) threshold was observed for Fe−CaP and Fe−CaP + Ge samples. The highest decrease was observed in the case of the Fe sample with the CaP coating, unlike the Fe−CaP + Ge, Fe−CaP + PEG, and Fe−CaP + Ge + PEG samples, confirming that the drug addiction does not result in a substantial decrease in viability compared to the control sample. This may be caused as a result of increased corrosion rate of the polymer-coated samples and the related pH change as well as the accumulation of degradation products of iron samples.[41] In the case of all samples after 4 and 24 h of cultivation, the cell viability stayed above the required level of 70%, suggesting that all samples were not toxic to the HDFa cells.[25]

**3.4. Antibacterial Activity.** The qualitative disc diffusion method was used to evaluate the antibacterial effect of CaP and CaP + Ge against *E. coli* (CCM 3954) and *S. aureus* (CCM 4223). The inhibitory activity was assessed by measuring the inhibition zones in millimeters. The control was an antibiotic disk containing 10 $\mu$g of gentamicin. The pure CaP coating did not show antibacterial activity, while the discs impregnated with CaP + Ge showed antibacterial activity against *E. coli* and *S. aureus* in concentrations from 6 to 0.75 mg/mL (Figure 9b). Lower concentrations no longer had an antibacterial effect. Gentamicin, an aminoglycoside with a high thermal stability, is a popular antibiotic for treating a variety of bacterial illnesses. Gentamicin has broad-spectrum efficacy against both Gram-negative bacteria like *E. coli* and Gram-positive bacteria like *S. aureus*.[45] The mechanism of action of gentamicin is dependent on inhibition of protein biosynthesis. Gentamicin inhibits bacterial protein synthesis due to binding to 16S rRNA on the 30S ribosomal subunit. The results showed that the CaP coating doped with gentamicin has a demonstrable antibacterial effect.[46]

**3.5. Gentamicin Release.** *3.5.1. Electroimpedance Spectroscopy and Conductivity Release.* For an evaluation of the release of gentamicin, conductivity measurements were performed in distilled water; the results are shown in Figure 10a. Based on the findings of the conductivity measurements of


https://doi.org/10.1021/acsomega.4c06192
ACS Omega 2024, 9, 48299−48314

the solution, a smooth increase in conductivity was observed throughout the hour, with no obvious decreases or increases in conductivity. However, it is possible to observe an increase in conductivity when comparing samples without and with the addition of gentamicin. This increase is much more prominent in the case of the samples that were coated with the PEG coating and in this case, the difference is about 14 $\mu$S/cm, while in the case of the samples that were coated only with the CaP coating, the difference was only 2 $\mu$S/cm. However, it is possible to observe an increase in conductivity when comparing samples without and with the addition of gentamicin. This increase is much more pronounced for samples coated with CaP + Ge coating; in this case, the difference is about 3.3 $\mu$S/cm, while for samples coated only with CaP coating, the difference was only 2.6 $\mu$S/cm. In the case of samples with CaP + PEG coating, the increase in conductivity was 1.4, and for the sample with CaP + Ge + PEG $\mu$S/cm coating, the increase was 2.1 $\mu$S/cm. This is a consequence of the reduced conductivity of the samples coated with the weakly conductive polymer coating and at the same time the increase of conductivity due to the conductive gentamicin. Based on the results, no detailed information about the processes on the phase interface is available.

Therefore, the release of gentamicin was studied by the EIS method. In the case of iron samples modified with Fe−CaP, Fe−CaP + Ge, Fe−CaP + PEG, and Fe−CaP + Ge + PEG, the Nyquist diagrams are shown in Figure 10b. Taking into consideration possible processes presented in the electrochemical system, there are more options. First, there is a release of gentamicin from the ceramic component into the solution. Gentamicin release could influence the conductivity of solution, but in this case, significant contribution to the conductivity is not expected since the PBS solution is quite conductive anyway. On the other hand, gentamicin integrated into the ceramic part could influence its conductivity such as in the case of doped materials. The second ongoing process is the gradual disintegration of the polymer film, but in such a short time horizon, it is unlikely that this would be an event that should significantly affect the results of the measurements. But the gentamicin release from the ceramic component could influence the polymer degradation, too. The release of gentamicin from the ceramic material can disrupt the polymer layer, which is present on top of the CaP.

EIS measurements were performed for 72 h in the PBS solution. Charge transfer resistance values were considered to study the behavior of various samples. The charge transfer resistances at the beginning of experiment were 71.67, 128.7, 74.79, and 1998 Ω for Fe−CaP, Fe−CaP + Ge, Fe−CaP + PEG, and Fe−CaP + Ge + PEG, respectively. For samples without the gentamicin, $R_{ct}$ decreases until 210 s (46.91 Ω) and 285 s (55.58 Ω) in case of Fe−CaP and Fe−CaP + PEG samples, respectively. Then $R_{ct}$ increases within 2 intervals; the first interval was from approximately 210 to 12,600 s and the second interval was up to 24 h for the Fe−CaP sample and up to 48 h in the case of the Fe−CaP-PEG sample. It could be expected that the increase of the charge transfer resistance values relates to the corrosion processes of the samples. In the case of sample Fe−CaP + PEG (1331 Ω after 72 h) was an increase of $R_{ct}$ higher than in the case of the Fe−CaP sample (792.8 Ω after 72 h). It means that more corrosion products are present on the surface of the sample, which corresponds to results of corrosion tests.

For samples with the gentamicin addition, different behavior was obtained. The charge transfer resistance increases until 5400 s (90 min) from 128.7 to 311.1 Ω in the case of the Fe−CaP + Ge sample. For sample Fe−CaP + Ge + PEG, $R_{ct}$ increases only 60 s from the 1998 Ω to 2237 Ω and then the values decrease to 285.1 Ω (after 10,800 s) and to 241.9 Ω (after 28,800 s). As was mentioned before, gentamicin release could influence the conductivity of sample, so the $R_{ct}$ decrease could be assigned to gentamicin release. Moreover, it could be concluded that the polymer layer on the top of the CaP + Ge component enhances the gradual gentamicin release (approximately 3 times longer in comparison to Fe−CaP + Ge). On the other hand, in the case of the sample Fe−CaP−PEG + Ge, gentamicin presence/release could influence the polymer layer stability and enhance polymer degradation due to its release from ceramic material through the polymer layer. At around 28,800 s, the values of charge transfer resistance are almost the same for the Fe−CaP + Ge and Fe−CaP + Ge + PEG samples. It could be expected that the sample surfaces are very similar to each other, so the assumption about PEG's faster degradation seems to be presumable. The values of the charge transfer resistance at 24 h are almost the same for all samples. After 48 h, an increase in $R_{ct}$ could be observed for Fe−CaP + Ge and Fe−CaP + Ge + PEG samples. The process of corrosion probably starts, and some corrosion products (less conductive in comparison to pure Fe) are present on the surface of the sample. Despite the samples displaying the same value of charge transfer resistance at 24 h, it could be assumed that the corrosion process is influenced by solution composition and other processes connected to previous modification of samples.

It could be concluded that for final modification of the Fe sample (Fe−CaP + Ge + PEG), each layer is important and fulfills its function for improvement of material properties. Based on the results, CaP anchors the gentamicin on the surface of the sample but enables its release into the solution. PEG enhances the corrosion of the prepared material and ensures gradual release of gentamicin during more than 8 h.

*3.5.2. UV−Vis Spectroscopy Measurements.* To verify the release of gentamicin from the coatings, the samples were put into 10 mL of PBS solution.

Gentamicin released into the solution was measured using a UV−vis spectrophotometer (Biochrom), where it showed maximum absorption at 291 nm (Figure 11a). Subsequently, the absorbance intensity was plotted as a function of the concentration of the gentamicin sulfate solution. The obtained calibration curve (Figure 11b) corresponds to the Beer−Lambert law, with a regression coefficient of 0.9944. Figure 12 shows the dependence of the amount of drug released from the coating as a function of time.

To correlate the in vitro drug release from the coating, the results were fitted to a suitable mathematical model. As shown in Figure 13, the fitted data for the Fe−CaP + Ge sample were best fit by the Higuchi model, with a correlation coefficient of 0.9239 (Figure 13b).

According to this model, in the case of a drug incorporated into a CaP coating, the liquid penetrates the coating and dissolves the embedded antibiotic; therefore, the drug release is diffusion-controlled in this case.

In the second case, when the drug was incorporated into the PEG coating, basic values of $n$ = 0.7801 were obtained, i.e., between 0.45 and 0.89 (Figure 14a), from the Korsmeyer−Peppas model with the highest correlation coefficient of


https://doi.org/10.1021/acsomega.4c06192
ACS Omega 2024, 9, 48299−48314

0.9287. In this case, drug release was controlled by polymer swelling, in addition to diffusion.

## 4. CONCLUSIONS

In order to minimize bacterial infections at implant locations, this study presents a unique bilayer ceramic and polymer coating for Fe-based biomaterials that not only speeds up degradation but also permits controlled, localized drug release. A ceramic CaP coating and a bioactive CaP + Ge coating were deposited on the surface of samples electrochemically in order to improve their biological properties. A polymer PEG coating was additionally applied to some of the samples in order to improve the degradation properties of iron biomaterials, which degrade very slowly.

Considering the facts obtained by studying these materials, it was found that samples with bilayer ceramic/polymer coating as well as bilayer drug-containing coating corroded faster compared to uncoated Fe samples and samples with a pure CaP and CaP + Ge coating.

Cell viability decreased with time, but for all samples, it was above 70% even after 24 h, so none of the samples were cytotoxic.

Based on tests of antibacterial activity against *E. coli* CCM 3954 and *S. aureus* CCM 4223, it was shown that the bioactive CaP + Ge coating showed antibacterial activity against both the *E. coli* and *S. aureus* bacterial strains. The pure CaP coating did not show an antibacterial activity.

A significant increase in conductivity was observed for samples with the bioactive drug (Ge) coating compared to that of drug-free samples, which was due to the release of conductive gentamicin from the surface of the samples.

To explain the release and to investigate the mechanism of drug release from the coatings, mathematical models were used to describe the drug release for CaP samples containing gentamicin as well as for CaP + Ge samples additionally covered with a polymeric PEG coating. Drug release in PBS solution is a process influenced by the nature of the drug, as well as individual coatings. Regression analysis showed that drug dissolution in PBS from CaP + Ge coatings was controlled by diffusion. In the case of CaP + Ge + PEG coatings, the process was influenced by polymer swelling, in addition to diffusion.

The beneficial properties of bilayer ceramic and polymer coatings have led to improved degradation properties and biocompatibility of Fe-based biomaterials. These materials represent promising possibilities, such as the possibility of adjusting the amount and time of drug release from the bioactive coating with the thickness of the upper polymer layer. By incorporating gentamicin into the bilayer coating, it also enables the creation of a high-performance bioactive coating for Fe bone implants with the ability to release the drug locally at the implant site in a controlled manner according to the patient's needs and at the same time prevent bacterial infection at the implantation site.

## ■ ASSOCIATED CONTENT

### Data Availability Statement

Data used to support the findings of this study are included in the article. If additional data or information is needed, these are available from the corresponding author upon request.

## ■ AUTHOR INFORMATION


### Corresponding Author

**Renáta Oriňaková** − *Department of Physical Chemistry, P. J. Šafárik University in Košice, 041 01 Košice, Slovakia; Centre of Polymer Systems, University Institute, Tomáš Bata University in Zlín, 76001 Zlín, Czech Republic;* orcid.org/0000-0001-8103-2634; Phone: +421-55-2342321; Email: renata.orinakova@upjs.sk; Fax: +421-55-6222124

### Authors

**Martina Petráková** − *Department of Physical Chemistry, P. J. Šafárik University in Košice, 041 01 Košice, Slovakia*

**Radka Gorejová** − *Department of Physical Chemistry, P. J. Šafárik University in Košice, 041 01 Košice, Slovakia*

**Jana Shepa** − *Department of Physical Chemistry, P. J. Šafárik University in Košice, 041 01 Košice, Slovakia*

**Ján Macko** − *Department of Physical Chemistry, P. J. Šafárik University in Košice, 041 01 Košice, Slovakia*

**Miriam Kupková** − *Institute of Materials Research, Slovak Academy of Sciences, 040 01 Košice, Slovakia*

**Ondrej Petruš** − *Institute of Materials Research, Slovak Academy of Sciences, 040 01 Košice, Slovakia*

**Matej Baláž** − *Institute of Geotechnics, Slovak Academy of Sciences, 040 01 Košice, Slovakia;* orcid.org/0000-0001-6563-7588

**Tibor Sopčák** − *Institute of Materials Research, Slovak Academy of Sciences, 040 01 Košice, Slovakia;* orcid.org/0000-0003-1818-8358

**Matej Mičušík** − *Institute of Polymers, Slovak Academy of Sciences, 845 41 Bratislava, Slovakia*

**Martin Kožár** − *Small Animal Clinic, The University of Veterinary Medicine and Pharmacy in Košice, 040 01 Košice, Slovakia*

**Vanda Hajdučková** − *Department of Microbiology and Immunology, University of Veterinary Medicine and Pharmacy in Košice, 041 81 Košice, Slovakia*

Complete contact information is available at: https://pubs.acs.org/10.1021/acsomega.4c06192


### Author Contributions

M.P: Writing, investigation, formal analysis, and visualization; R.G.: validation, investigation; J.S.: investigation and formal analysis; J.M.: investigation and methodology; M.K. (Miriam Kupková): investigation and methodology; O·P: investigation and formal analysis; M.B.: investigation and formal analysis; T.S: investigation and formal analysis; M.M.: investigation and formal analysis; R.O.: supervision. All authors have read and approved the final manuscript.

### Notes

The authors declare no competing financial interest.

## ■ ACKNOWLEDGMENTS

This work was supported by Project APVV-20-0278 of the Slovak Research and Development Agency, by the Internal scientific grant system of the Faculty of Natural Sciences UPJŠ in Košice (vvgs-2023-2518), by the Visegrad Grants from International Visegrad Fund (project no. 22310096) and by the EU NextGenerationEU through the Recovery and Resilience Plan for Slovakia under the project No. 09I03-03-V04-00010.



https://doi.org/10.1021/acsomega.4c06192
ACS Omega 2024, 9, 48299−48314

## REFERENCES


(1) Li, Q.; Jiang, G.; Wang, D.; Wang, H.; Ding, L.; He, G. Porous magnesium loaded with gentamicin sulphate and in vitro release behavior. *Mater. Sci. Eng. C* **2016**, *69*, 154−159.

(2) Gasior, G.; Szczepanski, J.; Radtke, A. Biodegradable iron-based materials what was done and what more can be done? *Materials* **2021**, *14*, 3381.

(3) Yusop, A. H. M.; Daud, N. M.; Nur, H.; Kadir, M. R. A.; Hermawan, H. Controlling the degradation kinetics of porous iron by poly(lactic-co-glycolic acid) infiltration for use as temporary medical implants. *Sci. Rep.* **2015**, *5*, 11194.

(4) Qi, Y.; Qi, H.; He, Y.; Lin, W.; Li, P.; Qin, L.; Hu, Y.; Chen, L.; Liu, Q.; Sun, H.; Liu, Q.; Zhang, G.; Cui, S.; Hu, J.; Yu, L.; Zhang, D.; Ding, J. Strategy of Metal-Polymer Composite Stent to Accelerate Biodegradation of Iron-Based Biomaterials. *ACS Appl. Mater. Interfaces* **2018**, *10*, 182−192.

(5) Gorejová, R.; et al. In vitro corrosion behavior of biodegradable iron foams with polymeric coating. *Materials* **2020**, *13*, 184.

(6) Mandracci, P.; Mussano, F.; Rivolo, P.; Carossa, S. Surface treatments and functional coatings for biocompatibility improvement and bacterial adhesion reduction in dental implantology. *Coatings* **2016**, *6*, 7.

(7) Rocha, D. N. d.; Silva, M. H. P. d.; Campos, J. B. d.; Marçal, R. L. S. B.; Mijares, D. Q.; Coelho, P. G.; Cruz, L. R. Kinetics of conversion of brushite coatings to hydroxyapatite in alkaline solution. *J. Mater. Res. Technol.* **2018**, *7*, 479−486.

(8) Djosic, M., S; Mitric, M.; Miskovic-Stankovic, V., B The porosity and roughness of electrodeposited calcium phosphate coatings in simulated body fluid. *J. Serb. Chem. Soc.* **2015**, *80*, 237−251.

(9) Djošić, M.; Janković, A.; Mišković-Stanković, V. Electrophoretic deposition of biocompatible and bioactive hydroxyapatite-based coatings on titanium. *Materials* **2021**, *14*, 5391.

(10) Pramanik, N.; Mishra, D.; Banerjee, I.; Maiti, T. K.; Bhargava, P.; Pramanik, P. Chemical Synthesis, Characterization, and Biocompatibility Study of Hydroxyapatite/Chitosan Phosphate Nanocomposite for Bone Tissue Engineering Applications. *Int. J. Biomater.* **2009**, *2009*, 1−8.

(11) Cheung, R. C. F.; Ng, T. B.; Wong, J. H.; Chan, W. Y. Chitosan: An update on potential biomedical and pharmaceutical applications. *Mar. Drugs* **2015**, *13*, 5156−5186.

(12) Zhu, X.; Whan Son, D.; Ong, J. L.; Kim, K. Characterization of hydrothermally treated anodic oxides containing Ca and P on titanium. *J. Mater. Sci.: Mater. Med.* **2003**, *14*, 629.

(13) *CHUSER 2012:2012 IEEE Colloquium on Humanities, Science & Engineering Research: Magellan Sutera Resort*, Institute of Electrical and Electronics Engineers, December 3−4, 2012, Kota Kinabalu, Sabah, Malaysia, 2012.

(14) Kar, A.; Raja, K. S.; Misra, M. Electrodeposition of hydroxyapatite onto nanotubular TiO2 for implant applications. *Surf. Coat. Technol.* **2006**, *201*, 3723−3731.

(15) Eliaz, N.; Eliyahu, M. Electrochemical processes of nucleation and growth of hydroxyapatite on titanium supported by real-time electrochemical atomic force microscopy. *J. Biomed. Mater. Res., Part A* **2007**, *80A*, 621−634.

(16) Ganvir, A.; Nagar, S.; Markocsan, N.; Balani, K. Deposition of hydroxyapatite coatings by axial plasma spraying: Influence of feedstock characteristics on coating microstructure, phase content and mechanical properties. *J. Eur. Ceram. Soc.* **2021**, *41*, 4637−4649.

(17) Sopyan, I.; Ramesh, S.; Nawawi, N. A.; Tampieri, A.; Sprio, S. Effects of manganese doping on properties of sol-gel derived biphasic calcium phosphate ceramics. *Ceram. Int.* **2011**, *37*, 3703−3715.

(18) Orinakovà, R.; Orinak, A.; Kupkovà, M.; Hrubovcàkovà, M.; Markusovà-Buckovà, L.; Giretovà, M.; Medvecky, L.; Dobrocka, E.; Petrus, O.; Kalavsky, F. In vitro degradation and cytotoxicity evaluation of iron biomaterials with hydroxyapatite film. *Int. J. Electrochem. Sci.* **2015**, *10*, 8158−8174.

(19) Geuli, O.; Metoki, N.; Zada, T.; Reches, M.; Eliaz, N.; Mandler, D. Synthesis, coating, and drug-release of hydroxyapatite nanoparticles loaded with antibiotics. *J. Mater. Chem. B* **2017**, *5*, 7819−7830.

(20) Pishbin, F.; Mouriño, V.; Flor, S.; Kreppel, S.; Salih, V.; Ryan, M. P.; Boccaccini, A. R. Electrophoretic deposition of gentamicin-loaded bioactive glass/chitosan composite coatings for orthopaedic implants. *ACS Appl. Mater. Interfaces* **2014**, *6*, 8796−8806.

(21) Zhang, S.; Cheng, X.; Shi, J.; Pang, J.; Wang, Z.; Shi, W.; Liu, F.; Ji, B. Electrochemical deposition of calcium phosphate/chitosan/gentamicin on a titanium alloy for bone tissue healing. *Int. J. Electrochem. Sci.* **2018**, *13*, 4046−4054.

(22) Hetrick, E. M.; Schoenfisch, M. H. Reducing implant-related infections: Active release strategies. *Chem. Soc. Rev.* **2006**, *35*, 780−789.

(23) *Standard Test Method for Conducting Potentiodynamic Polarization Resistance Measurements*; ASTM International, 2009. www.astm.org.

(24) ASTM G31 − 72, *ASTM G31: Standard Practice for Laboratory Immersion Corrosion Testing of Metals*, 2004.

(25) ISO-10993−5. *Biological evaluation of medical devices—part 5 tests for cytotoxicity: in vitro methods*. Arlington: ANSI/AAMI, 2009; pp 1−34.

(26) ISO 20645−2004, *Textile fabrics-Determination of antibacterial activity-Agar diffusion plate test*, 2004, pp 1−9. https://standards.iteh.ai/catalog/standards/sist/1fc097fa-f4b8-4d83-b10e-0d7ef158b13e/iso-20645-2004.

(27) Mendyk, A.; Jachowicz, R.; Fijorek, K.; Dorożyński, P.; Kulinowski, P.; Polak, S. KinetDS: An open source software for dissolution test data analysis. *Dissolution Technol.* **2012**, *19*, 6−11.

(28) Kormanová, V.; et al. Study of dissolution profiles of tramadolium chloride from controlled release dosage forms of matrix and reservoir type. *Ces. Slov. Farm.* **2010**, *59*, 210.

(29) Gergely, G.; Wéber, F.; Lukács, I.; Tóth, A. L.; Horváth, Z. E.; Mihály, J.; Balázsi, C. Preparation and characterization of hydroxyapatite from eggshell. *Ceram. Int.* **2010**, *36*, 803−806.

(30) Abifarin, J. K.; Obada, D. O.; Dauda, E. T.; Dodoo-Arhin, D. Experimental data on the characterization of hydroxyapatite synthesized from biowastes. *Data Brief* **2019**, *26*, 104485.

(31) Fu, X.; Kong, W.; Zhang, Y.; Jiang, L.; Wang, J.; Lei, J. Novel solid-solid phase change materials with biodegradable trihydroxy surfactants for thermal energy storage. *RSC Adv.* **2015**, *5*, 68881−68889.

(32) Bulina, N. V.; Makarova, S. V.; Baev, S. G.; Matvienko, A. A.; Gerasimov, K. B.; Logutenko, O. A.; Bystrov, V. S. A study of thermal stability of hydroxyapatite. *Minerals* **2021**, *11*, 1310.

(33) Taddei, P.; Affatato, S. Comparative Raman study on the molecular structure and IN VIVO wear of poly(methyl methacrylate)-based devices used as temporary knee prostheses: Effect of the antibiotic. *J. Mech. Behav. Biomed. Mater.* **2021**, *116*, 104328.

(34) Andrejovská, J.; Petruš, O.; Medveď, D.; Vojtko, M.; Riznič, M.; Kizek, P.; Dusza, J. Hardness and indentation modulus of human enamel and dentin. *Surf. Interface Anal.* **2023**, *55*, 270−278.

(35) Kuzmin, V. V.; Novikov, V. S.; Ustynyuk, L. Y.; Prokhorov, K. A.; Sagitova, E. A.; Nikolaeva, G. Y. Raman spectra of polyethylene glycols: Comparative experimental and DFT study. *J. Mol. Struct.* **2020**, *1217*, 128331.

(36) Beamson, G.; Briggs, D. High Resolution XPS of Organic Polymers: The Scienta ESCA300 Database. *J. Chem. Educ.* **1993**, *70*, A25.

(37) Haverová, L.; Oriňaková, R.; Oriňak, A.; Gorejová, R.; Baláž, M.; Vanýsek, P.; Kupková, M.; Hrubovčáková, M.; Mudroň, P.; Radoňák, J.; Országová Králová, Z.; Morovská Turoňová, A. An in vitro corrosion study of open cell Iron structures with PEG coating for bone replacement applications. *Metals* **2018**, *8*, 499.

(38) Oriňaková, R.; Gorejová, R.; Macko, J.; Oriňak, A.; Kupková, M.; Hrubovčáková, M.; Ševc, J.; Smith, R. M. Evaluation of in vitro biocompatibility of open cell iron structures with PEG coating. *Appl. Surf. Sci.* **2019**, *475*, 515−518.

(39) Oriňaková, R.; Gorejová, R.; Országová Králová, Z.; Haverová, L.; Oriňak, A.; Maskalová, I.; Kupková, M.; Džupon, M.; Baláž, M.;




https://doi.org/10.1021/acsomega.4c06192
*ACS Omega* 2024, 9, 48299−48314

Hrubovčáková, M.; Sopčák, T.; Zubrik, A.; Oriňak, M. Evaluation of mechanical properties and hemocompatibility of open cell iron foams with polyethylene glycol coating. *Appl. Surf. Sci.* **2020**, *505*, 144634.
(40) Oriňaková, R.; Oriňak, A.; Giretová, M.; Medvecký, L.; Kupková, M.; Hrubovčáková, M.; Maskal'ová, I.; Macko, J.; Kaľavský, F. A study of cytocompatibility and degradation of iron-based biodegradable materials. *J. Biomater. Appl.* **2016**, *30*, 1060−1070.
(41) Oriňaková, R.; Gorejová, R.; Čákyová, V.; Džupon, M.; Kupková, M.; Sopčák, T.; Özaltin, K.; Mičušík, M.; Petruš, O.; Omastová, M.; Vojtko, M.; Sáha, P. Biodegradable zinc-based materials with a polymer coating designed for biomedical applications. *J. Appl. Polym. Sci.* 2024, *141*, e54773.
(42) Guo, Y. P.; Guan, J. J.; Yang, J.; Wang, Y.; Zhang, C. Q.; Ke, Q. F. Hybrid nanostructured hydroxyapatite-chitosan composite scaffold: Bioinspired fabrication, mechanical properties and biological properties. *J. Mater. Chem. B* **2015**, *3*, 4679−4689.
(43) Wu, H. C.; Wang, T. W.; Sun, J. S.; Lee, Y. H.; Shen, M. H.; Tsai, Z. R.; Chen, C. Y.; Hsu, H. C. Development and characterization of a bioinspired bone matrix with aligned nanocrystalline hydroxyapatite on collagen nanofibers. *Materials* **2016**, *9*, 198.
(44) El Hadad, A. A.; Peón, E.; García-Galván, F.; Barranco, V.; Parra, J.; Jiménez-Morales, A.; Galván, J. Biocompatibility and corrosion protection behaviour of hydroxyapatite sol-gel-derived coatings on Ti6Al4V alloy. *Materials* **2017**, *10*, 94.
(45) Wojcik, M.; Kazimierczak, P.; Belcarz, A.; Wilczynska, A.; Vivcharenko, V.; Pajchel, L.; Adaszek, L.; Przekora, A. Biocompatible curdlan-based biomaterials loaded with gentamicin and Zn-doped nano-hydroxyapatite as promising dressing materials for the treatment of infected wounds and prevention of surgical site infections. *Biomater. Adv.* **2022**, *139*, 213006.
(46) Yazdimamaghani, M.; Razavi, M.; Vashaee, D.; Moharamzadeh, K.; Boccaccini, A. R.; Tayebi, L. Porous magnesium-based scaffolds for tissue engineering. *Mater. Sci. Eng. C* **2017**, *71*, 1253−1266.



https://doi.org/10.1021/acsomega.4c06192
*ACS Omega* 2024, 9, 48299−48314